POLITECNICO
MILANO 1863

SCUOLA DI INGEGNERIA INDUSTRIALE
E DELL'INFORMAZIONE

EXECUTIVE SUMMARY OF THE THESIS

Role of Hydrogeological Traits in Numerical Simulations of Aquifer Thermal Energy Storage

TESI MAGISTRALE IN ENERGY ENGINEERING – INGEGNERIA ENERGETICA

AUTHOR: MASOUD MANAFI

ADVISOR: FABIO INZOLI

CO-ADVISOR: EHSAN RANAEE

ACADEMIC YEAR: 2022-2023

1. Introduction

The heating and cooling storage system can hold promise in transitioning towards low-carbon energy sources, reducing reliance on fossil fuels for heating and cooling. Underground Thermal Energy Storage technologies, particularly Thermal Energy Storage (ATES), can effectively address fluctuations in energy availability and demand, making them vital components of sustainable energy systems. This research explores, in a numerical simulation framework, the feasibility of installing ATES systems within the diverse subsurface hydrogeological conditions of Milan metropolitan area.

Recently, energy demands in Milan metropolitan has been influenced by climate change, energy security concerns, and increased use of electrical appliances, necessitating efficient heating and cooling systems. ATES systems, despite some market-related barriers, can be an interesting potential solution.

Shallow aquifers in Milan metropolitan primarily fall into the categories of semi-confined or unconfined ones, with the latter experiencing fluctuations in water table levels influenced by factors like precipitation and groundwater extraction.

This study tries to conduct numerical simulations of ATES in shallow aquifers across three test cases, considering diverse hydrogeological conditions within Milan's metropolitan area. Utilizing data from selected locations, we create simplified box-model representations of confined and semi-confined aquifers. These models enable the

assessment of ATES system responses under varying complexity conditions, including rock properties, aquifer temperature, hydraulic gradients, rainfall recharge, and capillary pressure.

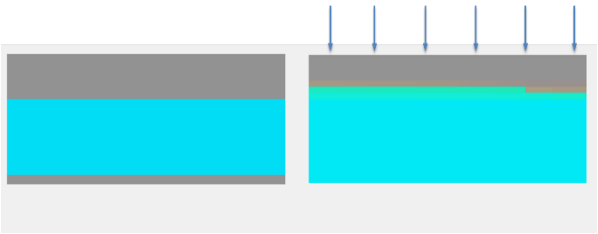

Figure 1. Schematic of confined (left) and semi-confined (right) simulation models.

The simulations are employed in ECLIPSE software environment, incorporating a black-oil formulation of the flow governing equations and energy conservation equations. The research can provide valuable insights into how shallow aquifer hydrogeological attributes may influence ATES performance and heat recovery efficiency.

2. Mathematical Framework and Governing Equations

All the simulations have been carried out using ECLIPSE 100 (E100) [Eclipse Reference Manual, 2023], which is developed to solve two-/three-phase flow problems in porous/fractured media. In the present study we use fully implicit method (available in E100) for discretizing and solving the governing two-phase (i.e., water/air) flow equations. In this study we advantage from a combination of coarsen and refined numerical mesh gridding. Refined grids are set in the area of interest (i.e., around wells) to increase accuracy of the simulation responses and the rest of model is grided coarsen to achieve faster simulations. While temperature plume is expected to be skewed in the direction of the natural flow refinement of the numerical cells around wells is shifted to the direction of the hydraulic gradient. In the confined models, refined grids are not assigned to the overburden as it does involve in thermal storage/production. Indeed, for semi-confined models, refinement of the numerical cells is extended to the unsaturated zone aiming to study effect of the capillary pressure and behaviour of the open aquifer in transient zone.

2.1. Governing equation

Groundwater flow and transport simulation inherently involve the consideration of multiple intricate factors that impact subsurface water system behaviour. Striking a balance between precision and simplicity is a pivotal challenge in groundwater modelling. In the absence of oil, formulation of two-phase (water-gas) fluid flow in porous media is presented here according to the following set of equations [e.g., Chen et al., 2006].

$$\frac{\partial}{\partial t}\left[\phi\left(\frac{S_\alpha}{B_\alpha}\right)\right] + \nabla\cdot\left(\frac{v_\alpha}{B_\alpha}\right) - \left(\frac{q_\alpha}{B_\alpha}\right) = 0 \;\; for \;\; \alpha = w, g \qquad (1)$$

$$\boldsymbol{v}_\alpha = -\frac{k_{r\alpha}\boldsymbol{k}}{\mu_\alpha}(\nabla p_\alpha - \rho_\alpha \nabla \wp z) \;\; for \;\; \alpha = w, g \qquad (2)$$

where $\alpha = \{w, g\}$ denote either water, w, or gas, g, phases; $\boldsymbol{k}$ is the absolute permeabilty tensor; ϕ is porosity; $\wp$ is gravity; z indicates a vertical coordinate; $q_{\alpha,s}$ is the source/sink term of phase α evaluated at stock tank conditions; S_α, p_α, μ_α, ρ_α, $k_{r\alpha}$, and $\boldsymbol{v}_\alpha$ respectively denote saturation, pressure, viscosity, density, relative permeability and Darcy velocity of the phase α at the reservoir conditions; B_α is the formation volume factor, and here $S_w + S_g = 1$. In the absence of oil for a water-air flow system (of the kind ATES simulations), reservoir densities of water, ρ_w, and gas (i.e., air), ρ_g, are computed from associated phase's surface densities (ρ_{sw}, ρ_{sg}) using following equations:

$$\rho_w = \frac{\rho_{w,s}}{B_w};\; \rho_g = \frac{\rho_{g,s}}{B_g} \qquad (3)$$

In E100 the well inflow/outflow performance relationship is set by using Peaceman (1978) model, in terms of the volumetric production rate of each phase at stock tank (standard surface pressure of 14.7 psi and temperature of 60 °F) conditions:

$$q_{\alpha,j} = \frac{\mathcal{C}\theta K_e}{ln(r_o/r_w)+S}\cdot\frac{K_{r\alpha,j}}{B_{\alpha,j}\mu_{\alpha,j}}\left(P_j - P_w - H_{w,j}\right) \qquad (4)$$

where $q_{\alpha,j}$ is the volumetric flow rate of phase α in connection j at stock tank conditions. The flow is taken as positive from the formation into the well, and negative from the well into the formation; $\mathcal{C}$ is a unit conversion factor (being 0.001127 in field

units' system), θ is the angle of the segment connecting with the well, in radians. In a Cartesian gridding its value is 6.2832 (=2π), as the connection is assumed to be in the center of the grid block, K_e is the effective permeability. For a vertical well the permeability used here is the geometric mean of the x- and y-direction permeabilities, $K_e = (K_x K_y)^{1/2}$, r_o is the "pressure equivalent radius" of the grid block (as defined below), r_w is the well bore radius, S is the skin factor (for the sake of simplicity we neglect the skin factor), $K_{r\alpha,j}$ is the relative permeability of the phase, $\mu_{\alpha,j}$ is the phase viscosity, and $B_{\alpha,j}$ is the phase formation volume factor, P_j is the nodal pressure in the grid block containing the connection, P_w is the bottom hole pressure of the well, $H_{w,j}$ is the well bore pressure head between the connection and the well's bottom hole datum depth.

For well model in Cartesian grid, the pressure equivalent radius of the grid block is defined as the distance from the well at which the local pressure is equal to the nodal average pressure of the block. By using Peaceman's formula which is applicable to rectangular grid blocks in which the permeability may be anisotropic.

$$r_o = 0.28 \frac{\left[D_x^2\left(\frac{K_y}{K_x}\right)^{1/2} + D_y^2\left(\frac{K_x}{K_y}\right)^{1/2}\right]^{1/2}}{\left(\frac{K_y}{K_x}\right)^{1/4} + \left(\frac{K_x}{K_y}\right)^{1/4}} \quad (5)$$

where; D_x and D_y are the x- and y- dimensions of the grid block, K_x and K_y are the x- and y- direction permeabilities.

The temperature option in E100 works as traces which enables E100 simulations to track temperature effects during reservoir simulations. To this end, energy conservation equation will be solved at the end of each numerical simulation timestep, and temperatures in the numerical grid blocks updates. The energy conversion equations are solved as a tracer while the tracer being the specific heat plus an additional (optional) term for heat conduction. Here, we introduced energy conservation equation available in E100 temperature option and then we explain each term within the non-linear residuals of the solutions. Conservation equation for energy (heat losses/gains not considered) can be presented as:

$$\frac{d}{dt}\Big(V_b \cdot \big((\rho_r c_{p,r} \cdot (1-\phi) \cdot \Delta T_c) + \sum \phi \cdot \Delta T_c \cdot \rho_\alpha \cdot c_{p,\alpha} \cdot S_\alpha\big)\Big) + \sum \Delta T_c \cdot \rho_\alpha \cdot c_{p,\alpha} \cdot q_\alpha + \Big(\Big(\phi \cdot \Big(\frac{\kappa_w + \kappa_g}{2}\Big) + (1-\phi) \cdot \kappa_r\Big) \cdot (\Delta T_{nc} - \Delta T_c) \cdot \mathcal{L}\Big) + \sum \Delta T_w \cdot \rho_\alpha \cdot c_{p,\alpha} \cdot q_\alpha = 0 \quad (6)$$

where ΔT_c, ΔT_{nc}, ΔT_w are temporal changes of temperature for each cell, neighboring cells, and well respectively; $q_{\alpha,c}$ is intercell flow rate of phase α; $\mathcal{L}$ is length of the cell; κ_r, κ_w, κ_g are thermal conductivity for rock water and gas respectively; ϕ is porosity; $c_{p,\alpha}$ and $c_{p,r}$ are specific heat for phase α and rock respectively; S_α is saturation for phase α. At each given simulation time step, when solution of the flow equation (1 to 4) is obtained (I.e., numerically converged) then equation (6) will be solved to evaluate ΔT. The block temperature is then updated by $T_{i+1} = T_i + \Delta T$. The major effect of temperature changes in the vicinity of the injection wells is to modify the fluid viscosities. Water viscosity values also update for the new values of temperature. The water viscosity at the prevailing temperature/pressure conditions, $\mu_w(T,P)$, is calculated as follows:

$$\mu_w(T,P) = \frac{\mu_w(T,P_{ref}) \times \mu_w(T_{ref},P)}{\mu_w(T_{ref},P_{ref})} \quad (7)$$

where $\mu_w(T_{ref},P_{ref})$ is the water viscosity at standard conditions; $\mu_w(T_{ref},P)$ is the water viscosity at a reference temperature; $\mu_w(T,P_{ref})$ is the water viscosity at a reference pressure; and P_{ref} is a reference pressure value.

2.2. Ordinary Kriging

The aim of kriging is to estimate the value of a given random variable, Z, at one or more unsampled points or over larger blocks, from more or less sparse sample data on a given support, let's say $z(\mathbf{x}_1)$, $z(\mathbf{x}_2)$, …, $z(\mathbf{x}_N)$ at points $\mathbf{x}_1$, $\mathbf{x}_2$, …, $\mathbf{x}_N$. The data may be distributed in one, two or three dimensions. Ordinary kriging (OK) is by far the most common type of kriging in environmental practices, and for this reason we focus on its theory (and application) here. OK relies on the assumption that we do not know the mean of property values. If we consider punctual estimation first, then we estimate Z at a point $\mathbf{x}_0$ by $\hat{Z}(\mathbf{x}_0)$, with the same support as the data, by:

$$\hat{Z}(\mathbf{x}_0) = \sum_{i=1}^{N} \lambda_i z(\mathbf{x}_i) \quad (8)$$

where λ_i are the weights. To ensure that the estimate is unbiased the weights are made to sum to 1, $\sum_{i=1}^{N} \lambda_i = 1$, and the expected error is $E\left[\hat{Z}(\mathbf{x}_0) - Z(\mathbf{x}_0)\right] = 0$. The estimation variance, var, is:

$$var\left[\hat{Z}(\mathbf{x}_0)\right] = E\left[\left\{\hat{Z}(\mathbf{x}_0) - Z(\mathbf{x}_0)\right\}^2\right] = 2\sum_{i=1}^{N} \lambda_i \gamma(\mathbf{x}_i, \mathbf{x}_0) - \sum_{i=1}^{N}\sum_{j=1}^{N} \lambda_i \lambda_j \gamma(\mathbf{x}_i, \mathbf{x}_j) \quad (9)$$

where $\gamma(\mathbf{x}_i, \mathbf{x}_j)$ is the semivariance of Z between the data points $\mathbf{x}_i$ and $\mathbf{x}_j$, and $\gamma(\mathbf{x}_i, \mathbf{x}_0)$ is the semivariance between the ith data point and the target point $\mathbf{x}_0$.

3. Simulation Model Setup

This orientation towards practical contexts directed the selection of focal regions, centered around three academic campuses: (a) Università degli Studi di Milano - Bicocca, situated in the Bicocca district of the North-Eastern Milan Metropolitan Area, (b) Università Commerciale Luigi Bocconi, positioned in the Porta Lodovica district within the Southern Milan Metropolitan Area, and (c) Politecnico di Milano, Bovisa Campus, sited in the Northern Milan Metropolitan Area's Bovisa district. Figure 2 illustrates three designated zones designated for on-site measurements, with the university campus locations marked as diminutive red squares.

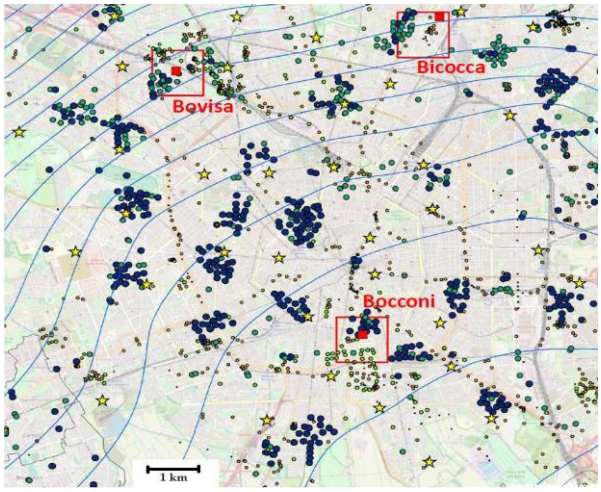

Figure 2. Location of interests in Milan, Italy.

In connection with on-site test data, the hydraulic conductivity values presented in Figures 3[De Caro et al., 2020] are obtained from the analysis of 8628 borehole logs, grain size distributions, and well tests. These measurements of hydraulic conductivity are pivotal in characterizing simulation models for Case A, Case B, and Case C.

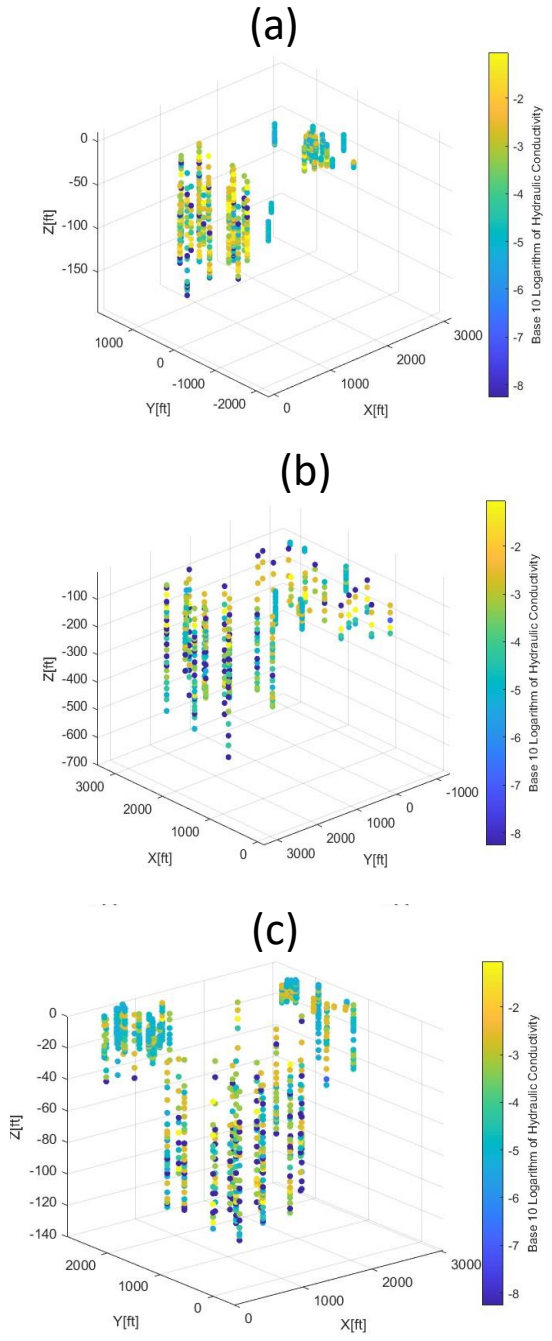

Figure 1. Hydraulic conductivity measured values in three case studies and used to characterize simulation model.

Permeability values are derived from hydraulic conductivity measurements using the subsequent equation [Freeze and Cherry, 1979]:

$$K_h = \frac{k\rho\wp}{\mu} \quad (10)$$

where K_h is the hydraulic conductivity, k is the permeability, ρ is the water density, $\wp$ is the acceleration due to gravity and μ is the water viscosity. In this context, a streamlined adaptation of the Kozeny-Carman equation is employed to characterize the porosity distribution [Ranaee et al., 2022]. Concretely, this correlation can be expressed as follows:

$$\phi = a \times [log_{10}^{K}] \quad (11)$$

In this context, where ϕ signifies porosity, K denotes permeability (measured in millidarcies), and a represents the cementation factor (a constant coefficient subject to variations based on the rock type), the relationship is characterized.

4. Results

This chapter is structured in three sections aiming to analyze the main aspects surrounding: (i) permeability field modelling through Kriging technique; (ii) responses of the ATES simulations to the imposed cyclic injection/production scenarios in terms of the expansion of the thermal plume; (iii) assessment of the recovery efficiency of the designed ATES system in the pilot cases.

4.1. Generating Permeability Filed

Hydraulic conductivity fields generated in SGeMS environment by using ordinary kriging (OK) estimation algorithm. Within the ordinary kriging method, measured data of hydraulic conductivity used as hard data and we used nugget effect of 0.3 to come up with reasonably good variograms. Because of the limited numbers of available measurements, the ellipsoid we used is relatively large (450 in each direction). Hydraulic conductivity values are then converted to evaluate permeability values via equation (10) and porosity values using empirical equation (11). Respecting the confined model, the permeability for underburden and overburden assumed to be mudstone, instead, for the aquifer itself permeability and porosity is characterized as homogeneous and assumed to be equal to the average permeability and porosity values of measurement data Figure 4 depict the permeability field for each case study further used to characterize E100 simulation model.

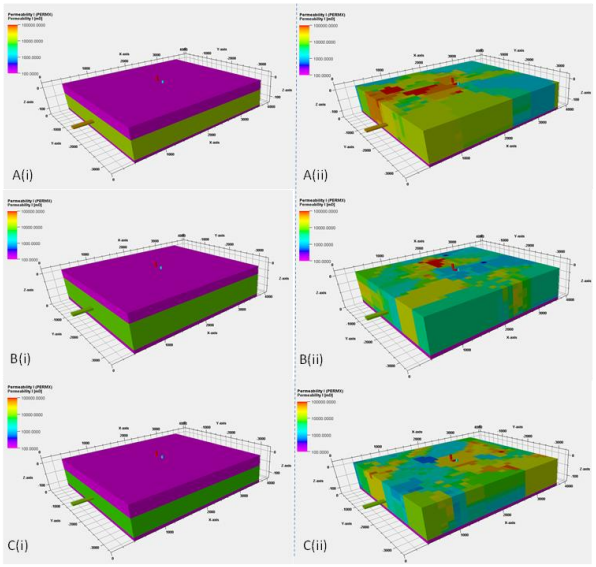

Figure 2. permeability field assigned to the: homogenous confined models (left column) and heterogenous semi-confined model (right column).

4.2. Thermal Simulation Response

As reported in Figure 5, the simulations have been set up to alternatively inject warm and cold water (each cycle switches in a six-month intervals).

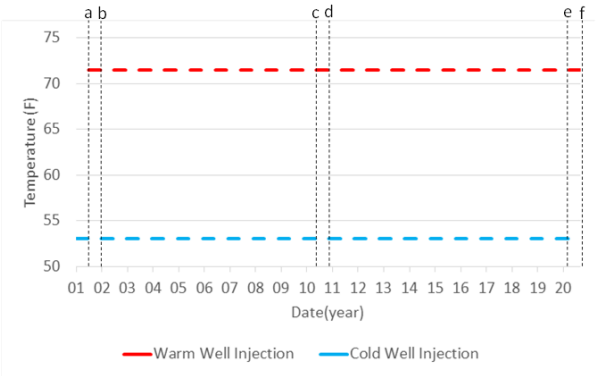

Figure 3. Water temperature assigned to the cycles scenario of warm/cold injection (with injection rate of 530 stb/day).

For case A, Figures 6 and 7 show the responses of the systems to the assigned seasonal cyclic injection/ production scenario in case A. Similar results of well temperature responses are reported for confined and semi-confined model. It is evident that the system can potentially gain advantages from a reduction in the injection temperature of the cold well. This advantage arises from the fact that

the reservoir temperature closely aligns with the prescribed temperature of the cold well.

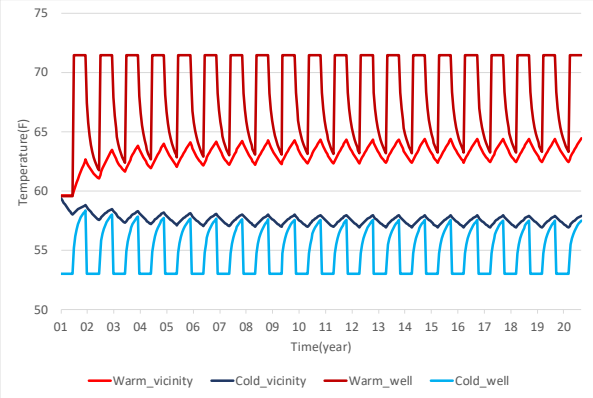

Figure 4. Temperature evolution in Wells head and field in vicinity of the wells, Case A confined.

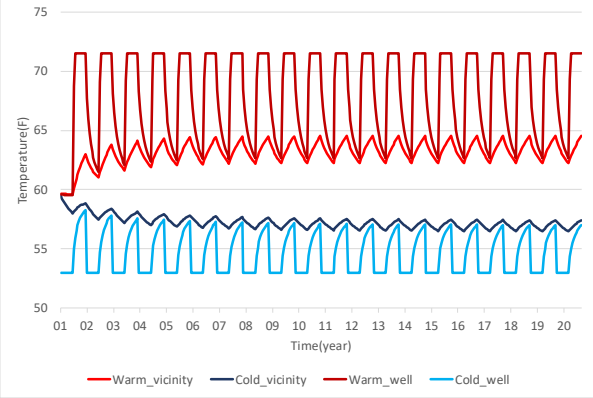

Figure 5. Temperature evolution in Wells head and field in vicinity of the wells, Case A semi-confined.

Figure 8 illustrates that the assignment of high permeability values and hydraulic gradients in case A results in the expansion of the thermal plume throughout the aquifer in the semi-confined model, particularly in the vicinity of the warm well. In contrast, the thermal plume exhibits less expansion in the confined model when it compared with the semi-confined model.

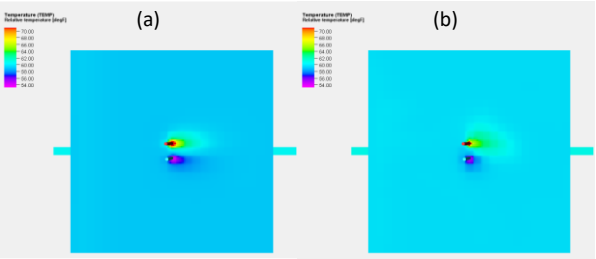

Figure 6. Case-A, Top view of temperature field after 20 years of simulation for confined (a) and semi-confined (b) models.

Figures 9 and 10 depict the system's reactions to the seasonal cyclic injection/production scenario in case B. A noteworthy observation is the relatively consistent pattern in the well temperature responses observed in both the confined and semi-confined models. In comparison to case A, it becomes apparent that case B demonstrates a more equitable response throughout the injection/production cycle. This observation implies that the system in case B is anticipated to exhibit more effective performance, with the field temperature gradually converging towards the well temperature as time progresses.

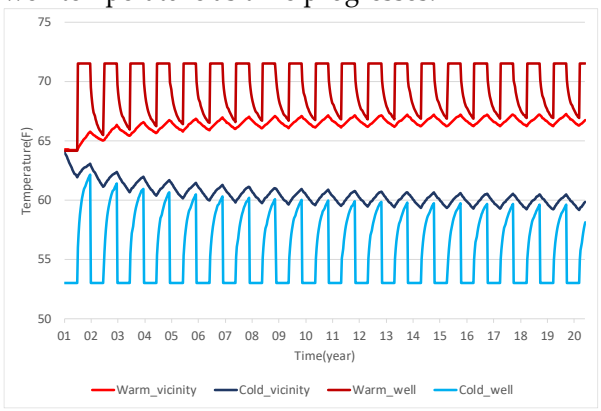

Figure 7. Temperature evolution in Wells head and field in vicinity of the wells, Case B confined.

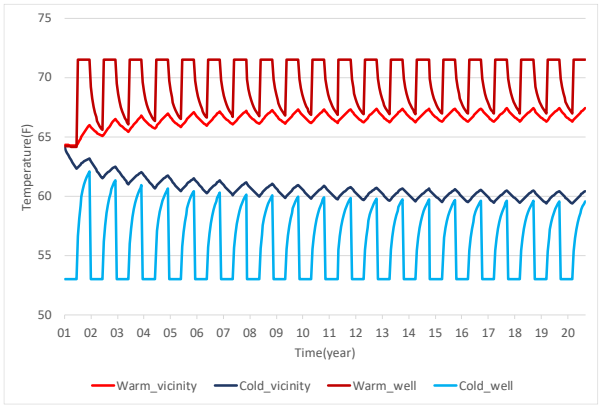

Figure 8. Temperature evolution in Wells head and field in vicinity of the wells, Case B semi-confined.

Figure 11 unmistakably illustrates a key difference compared to Case A. In Case B, the thermal plume does not disperse through natural flow, in contrast to the behavior observed in Case A. This divergence can be attributed to the lower permeability and hydraulic gradient characteristics associated with Case B.

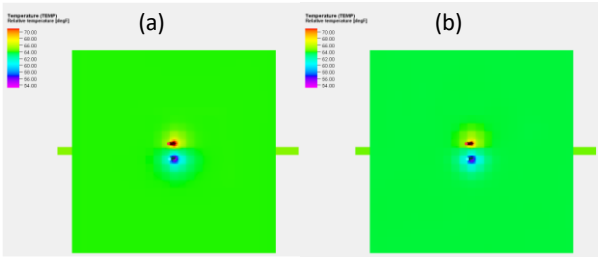

Figure 9. Case-B, Top view of temperature field after 20 years of simulation for confined (a) and semi-confined (b) models.

Similar to previous observations, a consistent pattern emerges in the well temperature responses within both the confined and semi-confined models in case C(figures 12 and 13). These figures underscore the potential advantages of reducing the injection temperature of the cold well. This benefit arises from the reservoir temperature closely aligning with the specified temperature of the cold well, indicating a promising avenue for enhancing the system's overall performance.

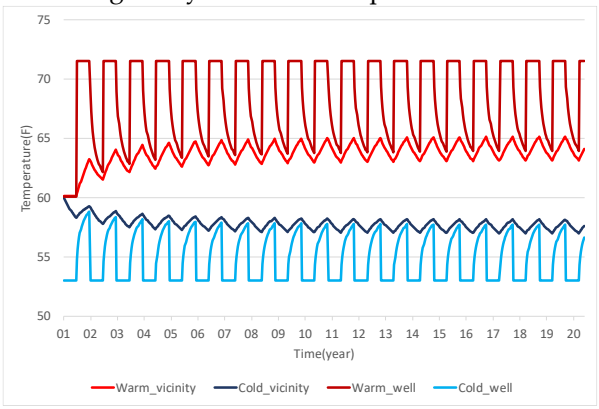

Figure 10. Temperature evolution in Wells head and field in vicinity of the wells, Case C confined.

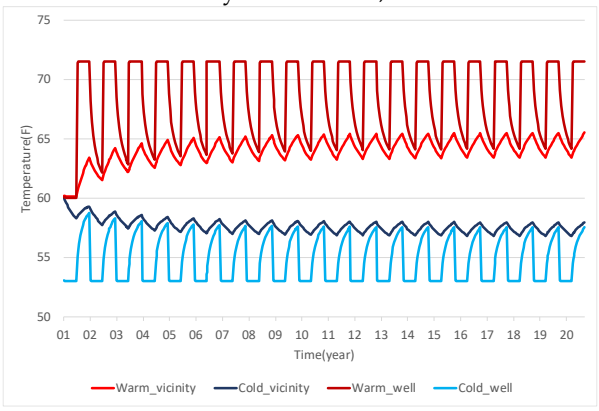

Figure 11. Temperature evolution in Wells head and field in vicinity of the wells, Case C – semi-confined.

As depicted in Figure 14, it is evident that the thermal plume expands more significantly within the natural flow direction in the semi-confined case, particularly near the warm well. This expansion is primarily attributable to the higher permeability observed in the vicinity of the warm well and the presence of a high hydraulic gradient in Case C. These factors collectively contribute to the enhanced movement and dispersion of the thermal plume in that direction.

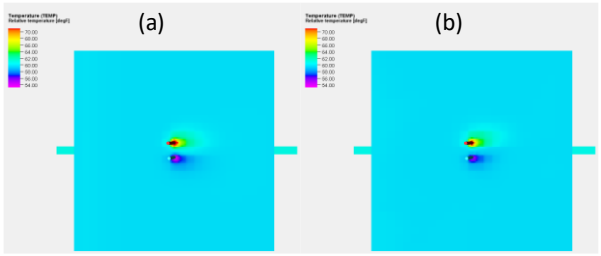

Figure 12. Case-C, Top view of temperature field after 20 years of simulation for confined (a) and semi-confined (b) models.

4.3. Thermal Recovery Efficiency

A commonly used approach to assess and compare the effectiveness of ATES systems across various contexts is through the utilization of Thermal Recovery Efficiency (or Thermal Recovery Factor), denoted as R_{th} [Sommer et al. in 2013];

$$R_{th} \triangleq \frac{\int_{Prod.} q_{prod}(T-T_n)\,dt}{\int_{Inj.} q_{inj}(T-T_n)\,dt} \qquad (12)$$

where T is the wellhead temperature, T_n the average initial undisturbed aquifer temperature over the well screen length and q_{inj} is the injection and q_{prod} is the production flow rates.

Following results involve a comparison of warm and cold well performances of five different models, starting with (i) a simple homogeneous confined model and progressing to (ii) semi-confined homogeneous, (iii) semi-confined heterogeneous, (iv) semi-confined heterogeneous models with inclusion of rainfall recharge effects, and finally, (v) a semi-confined full model that incorporates considerations of heterogeneity, rainfall recharge, and the influence of capillary pressure.

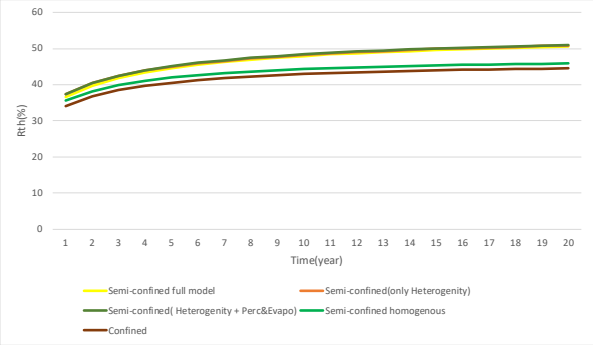

Figure 13. Cold Well Thermal Recovery Efficiency Bicocca Campus - Case A.

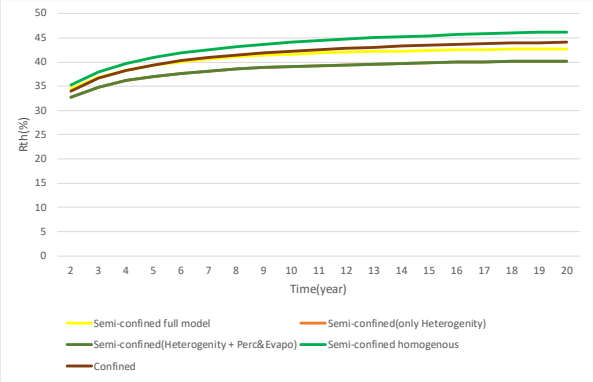

Figure 14. Warm Well Thermal Recovery Efficiency Bicocca Campus - Case A.

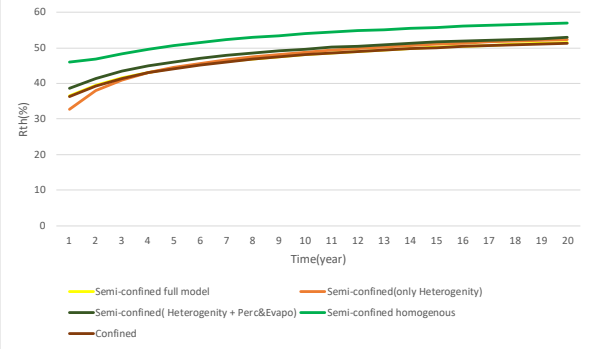

Figure 15. Cold Well Thermal Recovery Efficiency for Bocconi Campus - Case B.

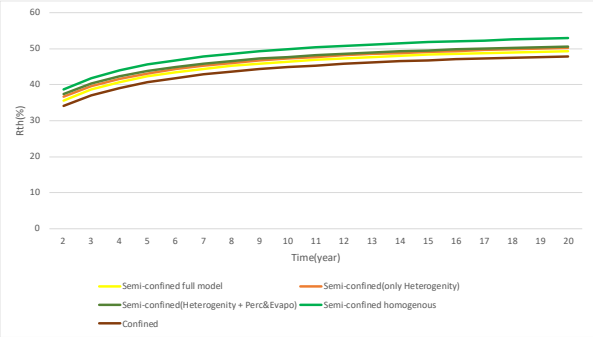

Figure 16. Warm Well Thermal Recovery Efficiency for Bocconi Campus - Case B.

Figure 17. Cold Well Thermal Recovery Efficiency for Bovisa Campus - Case C.

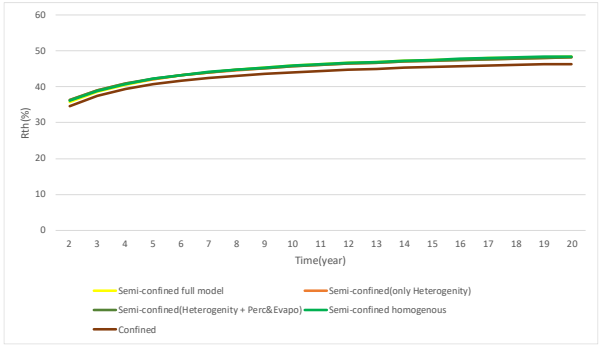

Figure 18. Warm Well Thermal Recovery Efficiency for Bovisa Campus - Case C.

5. Conclusions

This research offers a comprehensive exploration of Aquifer Thermal Energy Storage (ATES) systems, considering various hydrological factors. It begins with a simplified confined aquifer model, assuming homogeneity in rock attributes, and extends complexity to scenarios involving homogeneous semi-confined aquifers, heterogeneous semi-confined aquifers, and the effects of rainfall-induced recharge and capillary pressure.

Present study underscores the general potential of installing ATES systems in Milan's metropolitan area to address energy demands and reduce greenhouse gas emissions. The research demonstrates the importance of adapting thermal energy storage technologies to local hydrogeological conditions, offering sustainable solutions for heating and cooling needs in urban environments.

Employing E300's thermal license for more rigorous modeling and comparison with historical data, especially for more complex aquifers.

Key References

Eclipse Reference Manual, 2023.

Chen, Z., 2007. Reservoir simulation: mathematical techniques in oil recovery. Society for Industrial and Applied Mathematics.

Peaceman, D.W., 1978. Interpretation of well-block pressures in numerical reservoir simulation (includes associated paper 6988). Society of Petroleum Engineers Journal, 18(03), pp.183-194.

De Caro, M., Perico, R., Crosta, G. B., Frattini, P., Volpi, G., 2020. A regional-scale conceptual and numerical groundwater flow model in fluvio-glacial sediments for the Milan Metropolitan area (Northern Italy). Journal of Hydrology: Regional Studies Volume 29, June 2020, 100683. DOI:10.1016/j.ejrh.2020.100683;

Freeze, R. A., & Cherry, J. A., 1979. Groundwater. Prentice-Hall. DOI:10.1007/978-1-4020-6706-7;

Ranaee, E., Khattar, R., Inzoli, F., Blunt, M. J., Guadagnini, A., 2022. Assessment and uncertainty quantification of onshore geological CO2 storage capacity in China. International Journal of Greenhouse Gas Control 121 (2022) 103804. DOI:10.1016/j.ijggc.2022.103804;

Sommer, W., Valstar, J., Van Gaans, P., Grotenhuis, T., Rijnaarts, H., 2013. The impact of aquifer heterogeneity on the performance of aquifer thermal energy storage. Water Resources ResearchVolume 49, Issue 12 p. 8128-8138. DOI:10.1002/2013WR013677;